Contemporary Mathematics
https://ojs.wiserpub.com/index.php/CM/

UNIVERSAL WISER PUBLISHER

Research Article

Stagnation Point Flow and Heat Transfer on a Porous Stretching/Shrinking Cylinder: Analytical Procedure

Sina Sadighi, Marin Marin*

Department of Mathematics and Computer Science, Transilvania University of Brasov, Brasov, 500036, Romania
E-mail: m.marin@unitbv.ro

Received: 19 November 2025; **Revised:** 23 January 2026; **Accepted:** 26 January 2026

Abstract: This parametric study deals with stagnation point flow and heat transfer on a stretching/shrinking cylinder under convective boundary conditions. Unlike most existing investigations that rely on numerical or semi-analytical methods, closed-form parametric solutions are obtained for both the momentum and energy equations. It is based on the similarity solution that highly non-linear Partial Differential Equations (PDEs) can be reduced to highly non-linear Ordinary Differential Equations (ODEs). Suction/injection, curvature, stretching/shrinking, heat generation/absorption, radiation parameters, as well as Biot and Prandtl numbers are several parameters encountered in this problem. The energy equation is solved analytically using a confluent hypergeometric function, enabling explicit evaluation of temperature distributions and local Nusselt numbers. Plots and tables illustrate the velocity and temperature profiles, the local skin friction coefficient, and the Nusselt number. After analyzing the data in detail, it was found that a rise in the stretching parameter accelerates the growth rate in the local skin friction coefficient of the typical flow more than that of the stagnation point flow. Furthermore, the influence of the heat sink parameter is more prominent in high Biot numbers in order to achieve maximum local Nusselt numbers.

***Keywords*:** exact solutions, stagnation point flow, Biot number, porous cylinder, stretching/shrinking cylinder

MSC: 76N20, 76N15, 65L05, 34K06, 34K28

Nomenclature

a	Constant
Bi	Biot number
c_p	Specific heat at constant pressure
d	Stretching/shrinking parameter
k_f	Thermal conductivity of the fluid
k^*	Average absorption coefficient
Pr	Prandtl number
q_r	Radiative heat flux
Q_0	Heat source/sink
Q	Heat source/sink parameter

DOI: https://doi.org/10.37256/cm.7220269199

Rd	Radiation parameter
s	Suction/injection parameter
T_w	Fluid temperature at the wall
T_∞	Ambient temperature
u, v	Velocity component
v_w	Fluid mass at the wall

Greek letters

α	Thermal diffusivity
ζ	Intermediate variables
η	Similarity variable
γ	Curvature parameter
μ	Coefficient of fluid viscosity
v	Kinematic viscosity
ρ	Fluid density
σ	Electrical conductivity
σ^*	Stefan-Boltzmann constant

Subscripts

f	Fluid
w	Wall

1. Introduction

The concept of stagnation point flow can be defined as a specific type of fluid flow whereby the fluid velocity comes to a complete stop at a point or line on a surface. The point or line representing this stagnation is referred to as a stagnation point. It is worth mentioning that flow deflection, zero velocity, high pressure, and boosted heat and mass transfer are four key characteristics of stagnation point flow. Several disciplines take advantage of stagnation point flow applications. These include mechanical, chemical, industrial, and environmental engineering. They are also used to analyze the behavior of pollutants and contaminants in the air and water. A significant role is played by stagnation point flow in the design of aircraft and aerodynamic bodies. In order to optimize performance, it is necessary to analyze the flow around the stagnation point to determine drag forces and optimize the body shape. Several cooling and heating applications involve stagnation point flow. It is possible to cool electronic components and turbine blades efficiently with impinging jet cooling because of the high heat transfer coefficient at the stagnation point. Aeronautical engineers also utilize stagnation point flow to cool aircraft engines. Furthermore, there is also stagnation point flow in various parts of the cardiovascular system, including the bifurcation of blood vessels or the region surrounding the heart valves. Medical devices such as stents and artificial valves benefit from studying these flows, which provides insight into atherosclerosis (plaque buildup). Another application of stagnation point flow is in various chemical reactors and processes. When chemical vapor deposition is carried out on substrates, controlling the stagnation point helps to ensure uniform thin film deposition. In processes such as spray coating and electrospinning, a stagnation point flow is used.

The concept of stagnation point flow, while seemingly specific, is found across a wide range of contexts [1–3]. In the real world, stagnation point flow can be used in biological and environmental systems, microfluidic and lab-on-a-chip devices, and thermal systems. As a matter of fact, the aerospace and aviation industry is one of the most sensitive to stagnation point flow phenomena. The leading edge of wings and rockets experience stagnation point flow, for example. In order to calculate heat transfer, it's essential to keep this region in mind since it's often where the highest temperatures are created when the incoming air is compressed, which is critical for heat transfer calculations. Stagnation point flow problems can be solved analytically so that it can be determined which parameters have the most significant impact. Turkyilmazoglu and Pop [4] provided parametrical solutions for stagnation point flow and heat transfer on a porous stretching/shrinking sheet. Their investigation discussed various cases of stretching/shrinking strength parameters. Turkyilmazoglu [5] improved the previous paper and added slip velocity and magnetic field effects to the stagnation point flow. This study investigated two thermal boundary conditions: a constant wall temperature and a linearly increasing wall temperature. Mahabaleshwar et al. [6] provided exact solutions to the Casson fluid flow and radiative heat transfer on a porous stretching cylinder. According to the authors, there is an inverse relation between flow velocity with Casson and stretching parameters. An analysis was carried out by Awaludin et al. [7] involving a stagnation point flow on a porous stretching/shrinking cylinder with a prescribed heat flux thermal boundary condition. After analyzing stability, they concluded that the first solution is physically reliable and stable, whereas the second is not. An analysis of hybrid nanofluid flow on a stretching/shrinking cylinder was conducted by Waini et al. [8] using a numerical procedure. It has been shown in the research that curvature and nanoparticle volume fraction parameters are directly related to skin friction coefficient and heat transfer rate. A stagnation point flow on a non-porous shrinking cylinder has been investigated by Waini et al. [9] using the nanofluid effect. Another procedure to solve the Ordinary Differential Equations (ODEs) in boundary layer problems is to employ a semi-analytical method [10, 11]. Compared to numerical techniques, some pros of these methods include increased accuracy with fewer computations, a wide range of convergences, and series solutions for parametric studies. On the other hand, they also have some cons, such as series truncation errors, the requirement for analytical skills, and the complexity of implementation. A very popular geometry besides a sheet is a cylinder, which can also be converted to a sheet. The use of stretching/shrinking cylinders is widespread in various disciplines, including mechanical and biomedical engineering. An investigation of an unsteady biomagnetic flow on a porous stretching/shrinking cylinder was carried out by Ferdows et al. [12] using a numerical procedure. The authors declared that temperature distributions are directly related to radiation and unsteady parameters, regardless of whether porous cylinders stretch or shrink. Narayanaswamy et al. [13] reported that the Stefan blowing phenomenon has different effects on the heat and mass transfer rates. Allaw et al. [14] simulated an unsteady stagnation point flow problem on a porous stretching/shrinking sheet. After implementing a stability analysis, the authors concluded that the unsteady parameter is directly related to the local skin friction coefficient for both Single-Walled Carbon Nanotubes (SWCNTs) and Multi-Walled Carbon Nanotubes (MWCNTs) cases. The study by Najib et al. [15] involved a stagnation point flow on a non-porous stretching/shrinking cylinder, which was subjected to a first-order slip velocity effect. Slip velocity parameters affect the local skin friction coefficients and heat transfer rates in an inverse manner, as stated by the authors. Kandasamy et al. [16] used a hybrid nanofluid in an unsteady stagnation point flow over a moving cylinder. They displayed a direct relation between the temperature and concentration distributions with the Stefan blowing parameter. In recent years, scientists have developed hybrid nanofluid formulas, which offer several advantages over simple nanofluids [17–19]. Some pros could be summarized as enhanced stability, improved heat transfer performance, and cost-effectiveness. The magnetic field is one of the tools used to control flow in boundary layer problems. Makhdoum et al. [20] utilized a magnetic field and joule heating in a stagnation point flow on a porous stretching/shrinking cylinder. The numerical simulation conducted by Soomro et al. [21] focused on the flow of Magnetohydrodynamics (MHD) nanofluid through a porous stretching/shrinking cylinder. They employed a convective boundary condition for the energy equation and illustrated that the local Nusselt number directly relates to the suction/injection parameter. In his work, Alrehili [22] determined that velocity boundary layer thicknesses are inversely related to Hartmann number, suction, and Casson parameters. Furthermore, heat transfer rates are inversely related to the Hartmann number and Casson parameters. Another physical phenomenon is nonlinear thermal radiation, which is observed in combustion chambers of engines, spacecraft deployable structures, high-temperature material processing, and energy systems [23–25]. Cooler tooling or heat sinks could be used in order to conduct heat away from the thermal boundary layer. According to Li et al. [26], the Brownian motion parameter affects temperature and concentration distributions differently while inversely related to the heat transfer rate. Swain et al. [27] numerically analyze how nanoparticle aggregation influences the three-dimensional flow and heat transfer of a non-Newtonian (Maxwell) nanofluid over a permeable stretching surface, accounting for thermal radiation and internal heat generation/absorption. They solve the resulting coupled nonlinear equations to determine the effects on velocity, temperature, and skin friction profiles. Their results show that both radiation and aggregation significantly modify the fluid's thermal and momentum transport, offering insights relevant to engineering applications involving enhanced heat transfer in complex fluids. Recent years have seen many studies on boundary layer problems [28–32].

This investigation is needed to gain a better understanding of the fundamental physics behind this phenomenon. In addition, mathematical models are required for possible future applications. Although many exciting advances have been made in this area, unlike previous research that primarily relies on numerical or approximate techniques, this study provides exact analytical solutions for the velocity and temperature distributions in stagnation-point flow over a porous stretching/shrinking cylinder with convective boundary conditions. So, the main novelty of this study is to provide exact solutions to the momentum and energy equations of a stagnation point flowing on a stretching/shrinking cylinder. It is motivated by the extensive applications of stagnation point flow on a cylinder that has led to this study.

2. Mathematical formulation

An investigation of stagnation point flow on a porous stretching/shrinking cylinder is presented in this work. Thermal boundary conditions are convective, as shown in Figure 1. Also, heat generation/absorption and nonlinear thermal radiation phenomena are pictured.

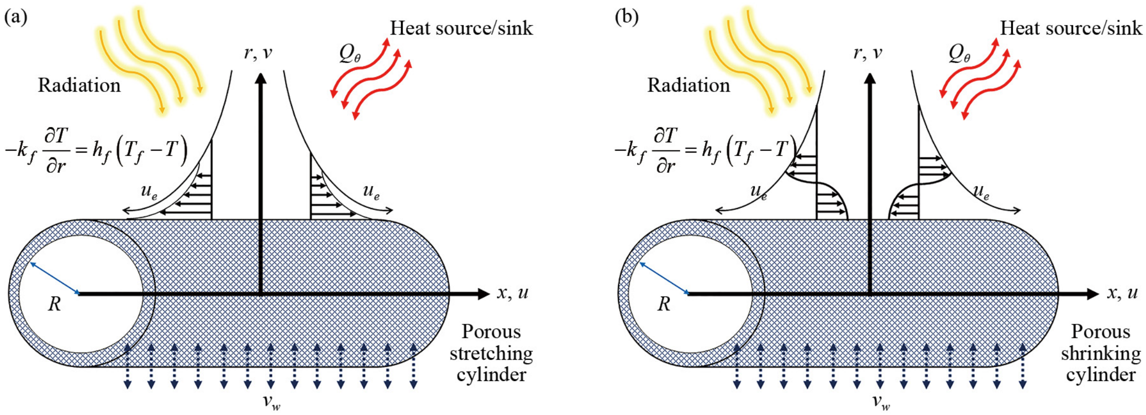

Figure 1. Schematic view of the problem (a) stretching case and (b) shrinking case

The governing equations of continuity, momentum, and energy in the boundary layer under the Rosseland approximation can be expressed as [33, 34]:

$$\frac{\partial (ru)}{\partial x} + \frac{\partial (rv)}{\partial r} = 0, \tag{1}$$

$$u\frac{\partial u}{\partial x} + v\frac{\partial u}{\partial r} = \frac{\mu_f}{\rho_f}\left(\frac{\partial^2 u}{\partial r^2} + \frac{1}{r}\frac{\partial u}{\partial r}\right), \tag{2}$$

$$(\rho c_p)_f\left(u\frac{\partial T}{\partial x} + v\frac{\partial T}{\partial r}\right) = k_f\left(\frac{\partial^2 T}{\partial r^2} + \frac{1}{r}\frac{\partial T}{\partial r}\right) + Q_0(T - T_\infty) - \frac{1}{r}\frac{\partial}{\partial r}(rq_r). \tag{3}$$

For completeness, the definitions of all variables and dimensionless parameters appearing in equations are summarized in the Nomenclature. In terms of relative heat flux, q_r represents the quantity. According to the Rosseland approximation, q_r can be expressed as follows:

$$q_r = -\frac{4\sigma^*}{3k^*}\frac{\partial T^4}{\partial r}. \tag{4}$$

Whereas k^* and σ^* are the Rosseland mean spectral absorption coefficient and Stefan-Boltzmann constant, respectively. In order to express a slight difference in the temperature, it is possible to expand T^4 with the help of the Taylor series (T_∞), so:

$$T^4 \cong 4T_\infty^3 T - 3T_\infty^4. \tag{5}$$

Upon inserting Eq. (5) into Eq. (4), the radiative heat flux can be expressed as follows:

$$q_r = -\frac{16\sigma^* T_\infty^3}{3k^*}\frac{\partial T}{\partial r}. \tag{6}$$

Differentiating the above equation gives the radiative term as follows:

$$\frac{\partial q_r}{\partial r} = -\frac{16\sigma^* T_\infty^3}{3K^*}\frac{\partial^2 T}{\partial r^2}. \tag{7}$$

Accordingly, the final expression of the energy equation in terms of a partial differential equation will be:

$$(\rho c_p)_f\left(u\frac{\partial T}{\partial x} + v\frac{\partial T}{\partial r}\right) = \left(k_f + \frac{16\sigma^* T_\infty^3}{3k^*}\right)\left(\frac{\partial^2 T}{\partial r^2} + \frac{1}{r}\frac{\partial T}{\partial r}\right) + Q_0\left(T - T_\infty\right). \tag{8}$$

In terms of boundary conditions, they are as follows:

$$r = R\begin{cases} u = u_w(x) = \lambda\dfrac{ax}{L},\ v = -V_w, \\ \\ -k_f\dfrac{\partial T}{\partial r} = h_f\left(T_w - T\right), \end{cases} \tag{9}$$

$$u \to \frac{ax}{L},\ T \to T_\infty \text{ as } r \to \infty. \tag{10}$$

The velocities in the $-x$ and $-r$ directions are u and v, respectively, and the fluid temperature is T. Furthermore, the porosity of the stretching/shrinking cylinder is represented by V_w. Considering the nature of the problem, the similarity variables have been chosen. In order to solve steady stagnation point flow and heat transfer on a porous stretching/shrinking cylinder, the appropriate similarity variables are [35]:

$$\eta = \frac{r^2 - R^2}{2R}\sqrt{\frac{a}{v_f L}},\ u = \frac{ax}{L}f'(\eta),\ v = -\frac{R}{r}\sqrt{\frac{av_f}{L}}f(\eta),\ \theta(\eta) = \frac{T - T_\infty}{T_w - T_\infty}. \tag{11}$$

There are several factors to consider when choosing the best similarity variables. Such as steady/unsteady, geometry, and boundary conditions. Accordingly, when PDEs are solved using similarity solutions, highly nonlinear coupled ODEs are obtained, as follows:

$$(1+2\gamma\eta)f''' + 2\gamma f'' + ff'' - f'^2 + r^2 = 0, \tag{12}$$

$$(1+Rd)(1+2\gamma\eta)\theta'' + (2+Rd)\gamma\theta' + Pr\left[f\theta' + Q\theta\right] = 0. \tag{13}$$

The transformed boundary conditions:

$$f(0) = s, \quad f'(0) = d, \quad \theta'(0) = -Bi(1+\theta(0)), \tag{14}$$

$$f'(\infty) \to r, \quad \theta(\infty) \to 0. \tag{15}$$

Partial Differential Equation (PDE) forms of the local skin friction coefficient and local Nusselt number are as follows [33, 34]:

$$C_f = \frac{\mu_f}{\rho_f u_w^2}\left(\frac{\partial u}{\partial r}\right)_{r=R}, \quad Nu_x = \frac{-x\left(k_f + \dfrac{16\sigma^* T_\infty^3}{3(\rho c_p)_f}\right)}{k_f(T_w - T_\infty)}\left(\frac{\partial T}{\partial r}\right)_{r=R}. \tag{16}$$

After using similarity variables, the Ordinary Differential Equation (ODE) forms of reduced local skin friction coefficient and local Nusselt number appear as follows:

$$Re_x^{1/2} C_f = f''(0), \quad Re_x^{-1/2} Nu_x = -(1+Rd)\theta'(0). \tag{17}$$

3. Analytical procedure

In order to satisfy the boundary conditions, the parametric solution to the ODEs can be written as follows [36]:

$$f(\eta) = s + r\eta + \frac{(d-r)}{\lambda}\left(1 - e^{-\lambda\eta}\right). \tag{18}$$

Once the above solution to Eq. (12) is inserted, the subsequent algebraic equation will be obtained:

$$[(1+2\gamma\eta)(d-r)]\lambda^2 - (2\gamma + s + r\eta)(d-r)\lambda - d^2 + r^2 = 0. \tag{19}$$

After solving the above equation with respect to the λ:

$$\lambda=\frac{2\gamma+s+r\eta\pm\sqrt{\eta^2r^2+2[\eta(2\gamma(2d+3r)+rs)+2(d+r)]+(s+2\gamma)^2}}{2(1+2\gamma\eta)}. \tag{20}$$

The first step in solving the energy equation (ODE form) analytically is to select a variable as an intermediate variable. Since the geometry is a cylinder, the new variable is $\zeta=-e^{-\lambda\eta}$ [37].

$$\zeta=-e^{-\lambda\eta} \text{ and } \frac{\partial\zeta}{\partial\eta}=-\lambda\zeta, \quad \frac{\partial\theta}{\partial\eta}=-\lambda\zeta\frac{\partial\theta}{\partial\zeta}, \quad \frac{\partial^2\theta}{\partial\eta^2}=\lambda^2\zeta\left(\zeta\frac{\partial^2\theta}{\partial\zeta^2}+\frac{\partial\theta}{\partial\zeta}\right). \tag{21}$$

Following the implementation of the above differentials into Eq. (13), the transformed and simplified ODE appears as follows:

$$\zeta\frac{\partial^2\theta}{\partial\zeta^2}+(1-C-x\zeta)\frac{\partial\theta}{\partial\zeta}+\left(\frac{q}{\zeta}\right)\theta=0. \tag{22}$$

Where:

$$C=\frac{(2+Rd)\gamma\lambda(1+2\gamma\eta)+Pr(s\lambda+d)}{(1+Rd)(1+2\gamma\eta)\lambda^2}, \quad x=\frac{\text{Prd}}{(1+Rd)(1+2\gamma\eta)\lambda^2}, \quad q=\frac{PrQ}{(1+Rd)(1+2\gamma\eta)\lambda^2}. \tag{23}$$

In this regard, the converted boundary conditions are:

$$\theta(0)=0, \quad \theta'(-1)=-\frac{Bi}{\lambda}[1-\theta(-1)]. \tag{24}$$

Eq. (22) is a kind of confluent hypergeometric differential equation, and since the equation is homogeneous, the solution contains one term. The boundary condition helps achieve the only coefficient (c_1) in the solution. The parametrical solution to the energy equation stands:

$$\theta(\eta)=c_1e^{-\lambda\eta^k}F\left(k,\ (k+1)(k+1-C)+q,\ -xe^{-\lambda\eta}\right). \tag{25}$$

The mathematical symbol $[F(\alpha,\ \beta,\ x)]$ represents the hypergeometric Kummer's function and $K=\dfrac{C+\sqrt{C^2-4q}}{2}$.

$$c_1=\frac{Bi}{(c_2+Bi)F\left(K,\ (K+1)^2-C(K+1)+q,\ -x\right)-c_3F\left(K-1,\ (K+1)^2-C(K+1)+q,\ -x\right)}. \tag{26}$$

Where:

$$c_2=\lambda\left[C(K+1)-K^2-x-q-1\right]+Bi, \quad c_3=\lambda[K(C-K-1)+C-q-1]. \tag{27}$$

4. Results and discussion

The problem concerns a stagnation point flow on a porous stretching/shrinking cylinder under radiation, heat source/sink, and convective boundary conditions. To obtain the exact solution, two mathematical procedures need to be followed. The first step involves converting the PDEs into ODEs using a similarity solution (results are shown in Section 2). The second one solves ODEs, as shown in Section 3. After analytically solving the equations in the previous section, this section represents the influences of parameters. The qualitative behavior of the velocity and temperature fields observed here is consistent with numerical findings reported for stagnation point flow over stretching/shrinking surfaces, thereby supporting the validity of the present analytical formulation.

Figure 2 shows the influence of suction/injection as well as stretching/shrinking parameters. When the suction parameter is increased and converted to an injection parameter, a higher velocity boundary layer thickness is obtained. Physically, adding fluid to the momentum boundary layer through the porous stretching/shrinking cylinder enhances outward momentum diffusion and raises the thickness. As a result, velocity adjustments occur over a wider radial extent when injection and stretching act simultaneously. A change in the stretching/shrinking parameter from 3 to 5 for $s = 2$ leads to an increase of 97.17% in the local skin friction coefficient. Furthermore, it is essential to note that the extent to which velocity boundary layer thickness is affected by stretching/shrinking parameters is highly significant.

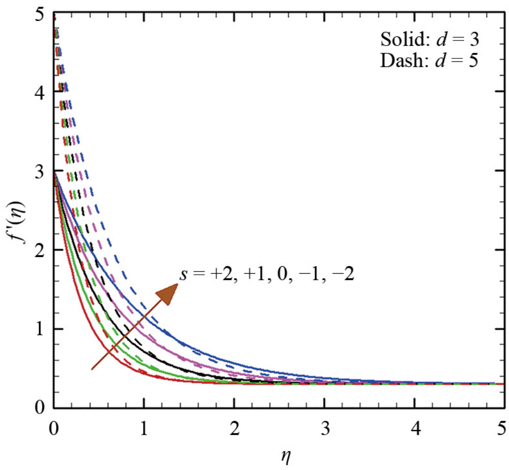

Figure 2. Effects of suction/injection and stretching/shrinking parameters on the velocity distribution when $\gamma = 0.1$ and $r = 0.3$

Figure 3 compares different cases, such as porous stretching/shrinking sheet with cylinder and stagnation point flow with typical fluid flow. The plot shows that stagnation point flows' Velocity Boundary Layer Thicknesses (VBLTs) are thicker than a typical fluid flow. Also, the velocity boundary layer increases in thickness by increasing the slight value of the velocity ratio parameter. Generally, the plot indicates that a cylinder produces thicker velocity boundary layer thicknesses than a sheet. Unlike a surface, the cylindrical geometry introduces radial variation in the shear distribution, redistributing momentum away from the wall as curvature increases. The velocity ratio parameter further controls the relative dominance of external stagnation flow versus surface-induced motion, explaining why curvature effects remain pronounced even at modest values of the velocity ratio. The local skin friction coefficient increases by 11.18% when γ is increased from 0 to 0.2 in the case of typical fluid flow ($r = 0$). Also, a rise in γ from 0 to 0.2 in stagnation point flow ($r = 0.2$) leads to an increment in the local skin friction coefficient by 10.87%. This shows that increasing these parameters equally (from 0 to 0.2) increases the curvature parameter's influence on the local skin friction coefficient more than the velocity ratio parameter's. Further, it is demonstrated that increasing both the curvature parameter and the velocity ratio parameter leads to an increasing and decreasing trend in the skin friction coefficient, respectively. The velocity boundary layer over a cylindrical surface is thicker than that over a flat sheet, primarily due to geometric curvature. In cylindrical coordinates, radial variations in the flow area cause the fluid to gradually redistribute momentum away from the surface, thereby reducing the effectiveness of wall-induced shear in confining the flow near the boundary. Unlike a flat sheet, where shear is uniformly distributed in the transverse direction, the cylinder's curvature introduces an additional radial divergence that weakens the velocity gradient near the wall. As a result, momentum diffuses over a larger radial distance, leading to a thicker velocity boundary layer for the cylindrical configuration.

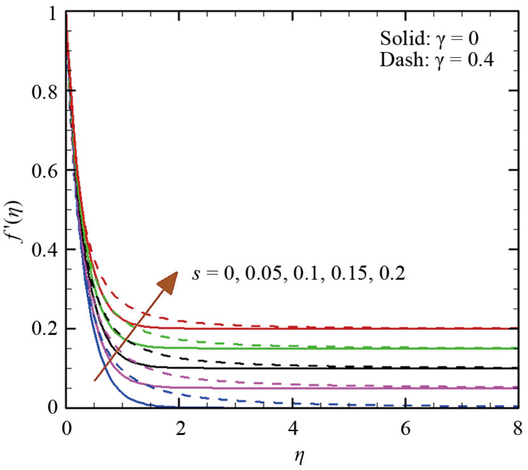

Figure 3. Effects of velocity ratio and curvature parameters on the velocity distribution when $s = 3$ and $d = 1$

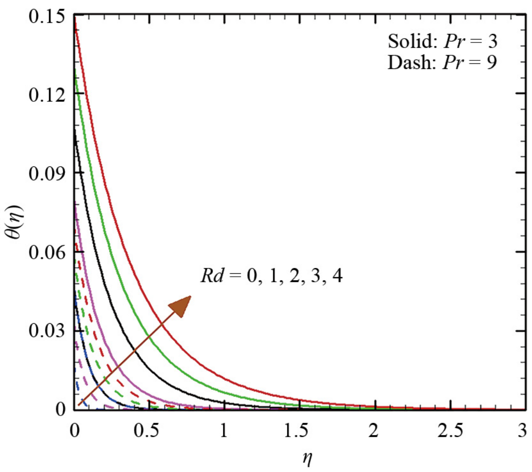

Figure 4. Effects of radiation parameter and Prandtl number on the temperature distribution when $s = 3$, $\gamma = 0.05$, $d = -1$, $r = 0.4$, $Q = -5$, and $Bi = 0.5$

Figure 4 illustrates the role of two parameters, the radiation parameter and the Prandtl number, in the energy equation. This plot demonstrates that the Temperature Boundary Layer Thickness (TBLT) rises with higher radiation parameters, contrary to the Prandtl number's trend. Increasing radiation parameters leads to the enhancement of fluid energy, thereby causing the TBLT to rise. On the other hand, the Prandtl number needs to be increased to achieve lower thermal boundary layer thicknesses. From an energy transport perspective, radiation introduces an additional heat transfer mechanism that functions independently of molecular conduction. This mechanism diminishes resistance to energy propagation within the thermal field, thereby rendering the temperature distribution less sensitive to local velocity gradients. In stagnation fluid flows with $Pr = 9$, viscosity effects are more prominent than they are in flows with $Pr = 3$, resulting in a greater disparity in heat transfer. Detailed analysis of this plot indicates that the local Nusselt number increases by 345% at $Pr = 3$ when the radiation parameter rises from 0 to 4 but increases by 373% at $Pr = 9$. This means that raising the Prandtl number leads to a rise in the local Nusselt number and also increases the rate of heat transfer.

Figure 5 depicts the quality and quantity of the heat source/sink parameter and Biot number on the temperature profile. Enhancing heat generation/absorption parameters from -2 to $+2$ under both cases ($Bi = 0.1$ and 0.9) results in increasing the thermal boundary layer thicknesses. As the plot shows, decreasing the Q value and shifting mode from the heat source to the heat sink are related to reducing the TBLT. Heat generation/absorption modifies the volumetric energy level within the boundary layer, whereas the Biot number determines the efficiency with which this energy imbalance is conveyed to the wall. In the case of increasing Q from -2 to $+2(200\%)$ at $Bi = 0.1$, the local Nusselt number decreases by 0.27%. Elevating the Biot number plays a significant role in internal conduction and surface convection, so the thermal boundary layer thicknesses will be thickened. It is also worth noting that increasing the Bi to 0.9 will reduce the local Nusselt number by 2.24%. So, to increase the heat transfer rate more, the magnitude of the heat sink parameter should be large, as should the Biot numbers.

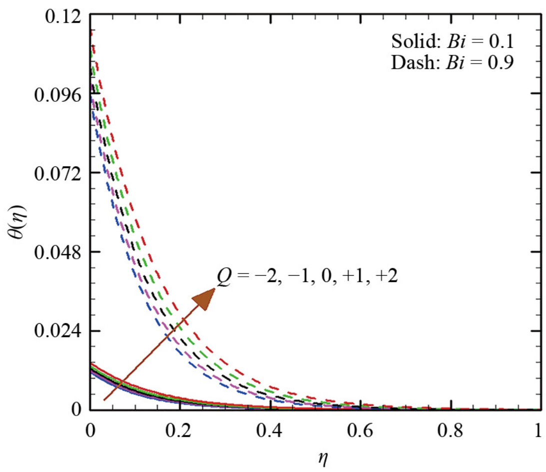

Figure 5. Effects of heat source/sink parameter and Biot number on the temperature distribution when $s = 2$, $\gamma = 0.08$, $d = 2$, $r = 0.1$, $Pr = 7$, and $Rd = 1$

Figure 6 shows the local skin friction coefficient as a function of stretching/shrinking and velocity ratio parameters. This plot implies that the local skin friction coefficient is more significant for stretching than for shrinking. In physical terms, the positive skin friction coefficient implies that shear stress occurs in the flow direction. Stretching enhances this alignment, thereby reinforcing the wall shear stress; in contrast, shrinking introduces opposing shear that partially counteracts the imposed strain rate. The velocity ratio parameter modulates this balance by regulating the relative influence of the free-stream stagnation flow on the development of the near-wall shear. According to the plot, normal fluid flow ($r = 0$) is characterized by a zero skin friction coefficient when d is zero, which signifies that when the cylinder switches from shrinking to stretching, the flow behavior shifts fundamentally. In Figure 7, the difference between heat sink and source parameters on local Nusselt numbers will become more evident as Biot increases. As a result, it seems clear that the Biot numbers are directly related to the local Nusselt numbers. From a physical standpoint, the difference in the local Nusselt number for the source or the sink seems to be at its lowest when Bi is at its lowest value and near zero due to its near uniform temperature. At elevated Biot numbers, the surface assumes the role of a more efficient conduit for energy exchange, rendering the heat transfer rate highly sensitive to whether thermal energy is introduced into or extracted from the boundary layer. This sensitivity decreases at low Biot numbers as a consequence of weaker wall-fluid thermal coupling.

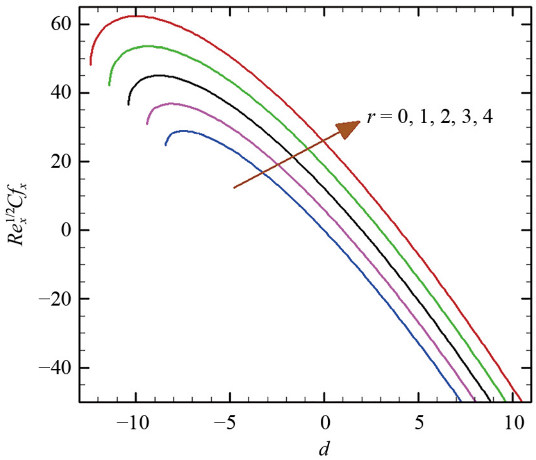

Figure 6. Effects of stretching/shrinking and velocity ratio parameters on the local skin friction coefficient when $s = 5$ and $\gamma = 0.4$

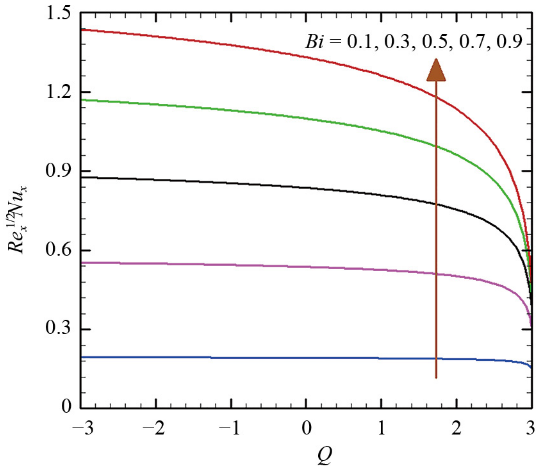

Figure 7. Effects of heat source/sink parameter and Biot number on the local Nusselt number when $s = -0.5$, $\gamma = 0.5$, $d = 10$, $r = 3$, $Pr = 4$, and $Rd = 1$

Figure 8 quantitatively shows the role of the suction/injection and velocity ratio parameters in the local skin friction coefficient. In Figure 8a, which represents the stagnation point flow, increasing d from 2 to 3 for $s = 2$ enhances the magnitude of the local skin friction coefficient by 3.47; in the meantime, for $s = 3.$ it rises to 4.20. On the other hand, for the typical fluid flow (Figure 8b), increasing d by 50% (from 2 to 3) increases the local skin friction coefficient for the lower suction parameter by 3.53 and for the higher one by 4.25. In stagnation point flow, the deceleration of fluid movement amplifies the influence of wall shear in the dissipation of momentum, thereby rendering skin friction more sensitive to variations in suction and stretching. In typical boundary layer flow, the lack of significant deceleration shifts the primary contribution to shear towards surface motion, thereby elucidating the comparatively greater sensitivity to stretching parameters.

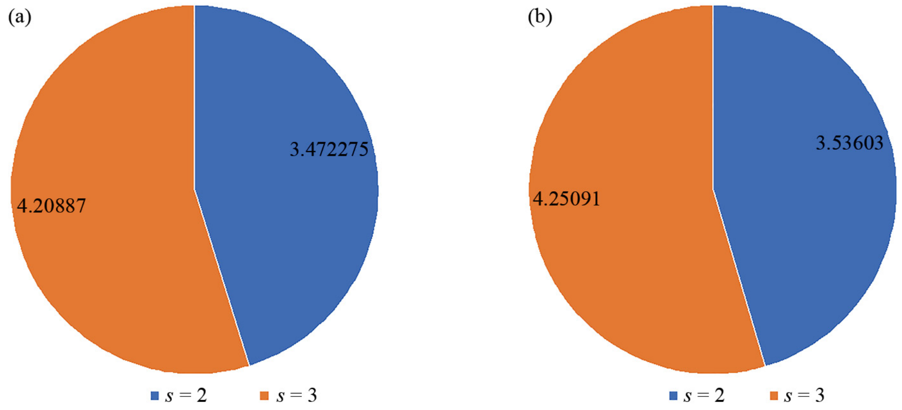

Figure 8. Increasing values of suction/injection, stretching/shrinking, and velocity ratio parameters on the local skin friction coefficient for (a) stagnation point flow ($r = 1$) and (b) typical fluid flow ($r = 0$) when $\gamma = 10^{-4}$

Table 1 demonstrates the behavior of the Prandtl number and radiation parameter on the cylinder when subjected to suction, stretching, stagnation point flow, and heat sink effects. As Prandtl numbers rise, the TBLT becomes thinner because the thermal diffusivity is reduced. This leads to a high-temperature gradient at the surface. As a result of the high gradient, the heat transfer rate is enhanced, which is reflected in a higher Nusselt number. As the Rd values increase, the effect becomes more apparent, pointing to an interaction between the Prandtl numbers and the radiation parameters. Following an analysis of the statistics, the percentage increase in Prandtl numbers from 5 to 7 at fixed radiation parameters ($Rd = 0,\ 1$, and 2) is 0.49%, 0.88%, and 1.2%, respectively. As Rd gets higher, the radiative heat flux goes up, which contributes to the total heat transfer from the surface. This importance is especially apparent in stagnation point flows where the flow slows down near the surface. Heat is transferred directly by radiation via electromagnetic waves, which increases local Nusselt numbers and overcomes this boundary layer limitation. Further analysis of the table reveals that when the radiation parameter changes from 0 to 2, with the Prandtl numbers fixed, the increasing percentage of the local Nusselt numbers is 191.2% for $Pr = 5$, 192.4% for $Pr = 6$, and 193.3% for $Pr = 7$, respectively. The table indicates that an increase in the Prandtl numbers on local Nusselt numbers is more noticeable at higher radiation parameter values. The following table illustrates a synergistic effect in which Rd amplifies the influence of Pr on the local Nusselt numbers. The increase in the local Nusselt numbers can be explained by a more pronounced increase in temperature gradient near the surface due to radiation raising the overall temperature gradient near the surface and a higher Pr, magnifying the gradient further.

Table 1. Variation of the local Nusselt number when $s = 5,\ \gamma = 10^{-4},\ d = 2,\ r = 0.2,\ Q = -10,\ Bi = 0.5$

Rd	Pr		
	5	6	7
0	0.4909	0.4923	0.4933
1	0.9665	0.9714	0.9750
2	1.4296	1.4394	1.4468

5. Conclusion

The stagnation point flow and heat transfer problem were solved using a combination of analytical procedures. The problem consists of a stagnation point flow containing radiative and heat source or sink phenomena on a porous stretching/shrinking cylinder under convective boundary conditions. The appropriate similarity variables considering the problem conditions were utilized to obtain exact solutions to the problem. The hypergeometric Kummer function was used to solve the energy equation under convective boundary conditions. The effects of parameters on profiles and coefficients are depicted and tabulated. According to the study, the following conclusions can be drawn:

• Velocity Boundary Layer Thicknesses (VBLTs) are directly influenced by s, r, and d parameters.

• The VBLTs of the cylinder are greater than those of the sheet.

• The Temperature Boundary Layer Thicknesses (TBLTs) thicken as Rd, Q parameters, and Biot number increase, while the Pr follows the opposite trend.

• The local skin friction coefficients become higher as the r and $-d$ parameters are increased.

• Bi and $+Q$ are directly and inversely related to the local Nusselt numbers, respectively.

• As the pie plot shows, the rate of increasing local skin friction coefficients in stagnation point flows is lower than that of typical flows.

Beyond its theoretical contribution, the present analysis holds significance for practical engineering systems involving stagnation point flow over cylindrical geometries, such as the cooling of cylindrical components, thermal processing, and fluid transport through porous surfaces. The incorporation of convective boundary conditions, radiation, and internal heat generation/absorption significantly improves the relevance of the results to real thermal environments encountered in energy, chemical, and mechanical engineering disciplines. Furthermore, the provision of exact analytical solutions furnishes dependable benchmark outcomes that can be utilized to validate numerical simulations and approximation techniques, thereby offering a more profound understanding of parameter sensitivity devoid of discretization or convergence ambiguities.

Data availability

The datasets used and/or analyzed during the current study available from the corresponding author on reasonable request.

Conflict of interest

The authors declare no competing financial interest.

References

[1] Adigun JA, Adeniyan A, Abiala IO. Stagnation point MHD slip-flow of viscoelastic nanomaterial over a stretched inclined cylindrical surface in a porous medium with dual stratification. *International Communications in Heat and Mass Transfer*. 2021; 126: 105479. Available from: https://doi.org/10.1016/j.icheatmasstransfer.2021.105479.

[2] Choudhary S, Choudhary P, Alessa N, Loganathan K. MHD thermal and solutal stratified stagnation flow of tangent hyperbolic fluid induced by stretching cylinder with dual convection. *Mathematics*. 2023; 11(9): 2182. Available from: https://doi.org/10.3390/math11092182.

[3] Ghazali NMS, Abd Aziz AS, Soid SK, Ilias MR, Ali ZM. Stagnation point flow in copper nanofluid over slippery cylinder with viscous dissipation. *Journal of Physics: Conference Series*. 2021; 1770(1): 012041. Available from: https://doi.org/10.1088/1742-6596/1770/1/012041.

[4] Turkyilmazoglu M, Pop I. Exact analytical solutions for the flow and heat transfer near the stagnation point on a stretching/shrinking sheet in a Jeffrey fluid. *International Journal of Heat and Mass Transfer*. 2013; 57(1): 82-88. Available from: https://doi.org/10.1016/j.ijheatmasstransfer.2012.10.006.

[5] Turkyilmazoglu M. Magnetic field and slip effects on the flow and heat transfer of stagnation point Jeffrey fluid over deformable surfaces. *Zeitschrift for Nature Research A*. 2016; 71(6): 549-556. Available from: https://doi.org/10.1515/zna-2016-0047.

[6] Mahabaleshwar US, Maranna T, Mishra M, Hatami M, Sunden B. Radiation effect on stagnation point flow of Casson nanofluid past a stretching plate/cylinder. *Scientific Reports*. 2024; 14(1): 1387. Available from: https://doi.org/10.1038/s41598-024-51963-2.

[7] Awaludin IS, Ahmad R, Ishak A. On the stability of the flow over a shrinking cylinder with prescribed surface heat flux. *Propulsion and Power Research*. 2020; 9(2): 181-187. Available from: https://doi.org/10.1016/j.jppr.2020.03.001.

[8] Waini I, Ishak A, Pop I. Hybrid nanofluid flow on a shrinking cylinder with prescribed surface heat flux. *International Journal of Numerical Methods for Heat and Fluid Flow*. 2021; 31(6): 1987-2004. Available from: https://doi.org/10.3390/sym12091493.

[9] Waini I, Ishak A, Pop I. Nanofluid flow on a shrinking cylinder with Al_2O_3 nanoparticles. *Mathematics*. 2021; 9(14): 1612. Available from: https://doi.org/10.3390/math9141612.

[10] Rashid U, Liang H, Ahmad H, Abbas M, Iqbal A, Hamed YS. Study of (Ag and TiO_2)/water nanoparticles shape effect on heat transfer and hybrid nanofluid flow toward stretching shrinking horizontal cylinder. *Results in Physics*. 2021; 21: 103812. Available from: https://doi.org/10.1016/j.rinp.2020.103812.

[11] Cham A, Mustafa M. Examining stagnation-point flow impinging on a deforming cylinder in Reiner-Rivlin fluid with integrated heat and mass transfer. *Case Studies in Thermal Engineering*. 2024; 60: 104598. Available from: https://doi.org/10.1016/j.csite.2024.104598.

[12] Ferdows M, Alam J, Murtaza G, Tzirtzilakis EE, Sun S. Biomagnetic flow with $CoFe_2O_4$ magnetic particles through an unsteady stretching/shrinking cylinder. *Magnetochemistry*. 2022; 8(3): 27. Available from: https://doi.org/10.3390/magnetochemistry8030027.

[13] Narayanaswamy MK, Kandasamy J, Sivanandam S. Go-MoS_2/water flow over a shrinking cylinder with Stefan blowing, Joule heating, and thermal radiation. *Mathematical and Computational Applications*. 2022; 27(6): 110. Available from: https://doi.org/10.3390/mca27060110.

[14] Allaw D, Bachok N, Arifin NM, Ali FM. Double solutions of unsteady stagnation-point of carbon nanotubes across a permeable exponential stretching/shrinking sheet. *Chinese Journal of Physics*. 2023; 85: 534-552. Available from: https://doi.org/10.1016/j.cjph.2023.03.018.

[15] Najib N, Bachok N, Dzulkifli NF, Pop I. Numerical results on slip effect over an exponentially stretching/shrinking cylinder. *Mathematics*. 2022; 10(7): 1114. Available from: https://doi.org/10.3390/math10071114.

[16] Kandasamy J, Narayanaswamy MK, Sivanandam S. Effects of variable viscosity in unsteady magnetohydrodynamic hybrid nanofluid flow over stretching/shrinking cylinder with partial slip and Stefan blowing. *Nanomanufacturing*. 2023; 3(4): 434-445. Available from: https://doi.org/10.3390/nanomanufacturing3040027.

[17] Zainal NA, Waini I, Khashi'ie NS, Kasim ARM, Naganthran K, Nazar R, et al. Stagnation point hybrid nanofluid flow past a stretching/shrinking sheet driven by Arrhenius kinetics and radiation effect. *Alexandria Engineering Journal*. 2023; 68: 29-38. Available from: https://doi.org/10.1016/j.aej.2023.01.005.

[18] Yasir M, Malik ZU, Alzahrani AK, Khan M. Study of hybrid Al_2O_3-Cu nanomaterials on radiative flow over a stretching/shrinking cylinder: Comparative analysis. *Ain Shams Engineering Journal*. 2023; 14(9): 102070. Available from: https://doi.org/10.1016/j.asej.2022.102070.

[19] Fadhel MA, Asghar A, Lund LA, Shah Z, Vrinceanu N, Tirth V. Dual numerical solutions of Casson SA-hybrid nanofluid toward a stagnation point flow over stretching/shrinking cylinder. *Nanotechnology Reviews*. 2024; 13(1): 20230191. Available from: https://doi.org/10.1515/ntrev-2023-0191.

[20] Makhdoum BM, Mahmood Z, Khan U, Fadhl BM, Khan I, Eldin SM. Impact of suction with nanoparticles aggregation and Joule heating on unsteady MHD stagnation point flow of nanofluids over horizontal cylinder. *Heliyon*. 2023; 9(4): e15012. Available from: https://doi.org/10.1016/j.heliyon.2023.e15012.

[21] Soomro AM, Fadhel MA, Lund LA, Shah Z, Alshehri MH, Vrinceanu N. Dual solutions of magnetized radiative flow of Casson nanofluid over a stretching/shrinking cylinder: Stability analysis. *Heliyon*. 2024; 10(8): e29696. Available from: https://doi.org/10.1016/j.heliyon.2024.e29696.

[22] Alrehili M. Nanofluid dissipative stagnation point flow of Casson type over a stretched sheet influenced by a variable surface heat flux and magnetic field. *Results in Physics*. 2024; 58: 107535. Available from: https://doi.org/10.1016/j.rinp.2024.107535.

[23] Madhu J, Madhukesh JK, Sarris I, Prasannakumara BC, Ramesh GK, Shah NA, et al. Influence of quadratic thermal radiation and activation energy impacts over oblique stagnation point hybrid nanofluid flow across a cylinder. *Case Studies in Thermal Engineering*. 2024; 60: 104624. Available from: https://doi.org/10.1016/j.csite.2024.104624.

[24] Khan SA, Ramzan A, Ali M, Imran M, Machado JM, Kedzia K, et al. Numerical simulation of bioconvection Maxwell nanofluid flow due to stretching/shrinking cylinder with gyrotactic motile microorganisms: A biofuel applications. *BioNanoScience*. 2024; 14(5): 4895-4909. Available from: https://doi.org/10.1007/s12668-024-01516-8.

[25] Karthik G, Kumar PV. EMHD stagnation point flow of dusty hybrid nanofluid over a permeable stretching sheet: Radiative solar applications. *Case Studies in Thermal Engineering*. 2024; 54: 104044. Available from: https://doi.org/10.1016/j.csite.2024.104044.

[26] Li S, Faizan M, Ali F, Ramasekhar G, Muhammad T, Khalifa HAEW, et al. Modelling and analysis of heat transfer in MHD stagnation point flow of Maxwell nanofluid over a porous rotating disk. *Alexandria Engineering Journal*. 2024; 91: 237-248. Available from: https://doi.org/10.1016/j.aej.2024.02.002.

[27] Swain K, Ibrahim SM, Dharmaiah G, Noeiaghdam S. Numerical study of nanoparticles aggregation on radiative 3D flow of Maxwell fluid over a permeable stretching surface with thermal radiation and heat source/sink. *Results in Engineering*. 2023; 19: 101208. Available from: https://doi.org/10.1016/j.rineng.2023.101208.

[28] Marin M. On existence and uniqueness in thermoelasticity of micropolar bodies. *Proceedings of the French Academy of Sciences, Series II*. 1995; 321(12): 475-480.

[29] Marin M, Florea O. On temporal behaviour of solutions in thermoelasticity of porous micropolar bodies. *Annals of the Ovidius University of Constanta-Mathematics Series*. 2014; 22(1): 169-188. Available from: https://doi.org/10.2478/auom-2014-0014.

[30] Ahmed S, Chen ZM, Xu H, Ishaq M. Mixed convection flow in a square lid-driven cavity subject to inclined magnetic field with highly accurate wavelet-homotopy solutions. *Computers and Mathematics with Applications*. 2024; 162: 33-51. Available from: https://doi.org/10.1016/j.camwa.2024.03.005.

[31] Ahmed S, Xu H. Mixed convection in gravity-driven thin nano-liquid film flow with homogeneous-heterogeneous reactions. *Physics of Fluids*. 2020; 32(2): 023101. Available from: https://doi.org/10.1063/1.5140366.

[32] Ahmed S, Chen ZM, Ishaq M. Multiple solutions in magnetohydrodynamic stagnation flow of hybrid nanofluid past a sheet with mathematical chemical reactions model and stability analysis. *Physics of Fluids*. 2023; 35(7): 073102. Available from: https://doi.org/10.1063/5.0157429.

[33] Khan MR, Puneeth V, Alaoui MK, Alroobaea R, Abdou MMM. Heat transfer in a dissipative nanofluid passing by a convective stretching/shrinking cylinder near the stagnation point. *ZAMM-Journal of Applied Mathematics and Mechanics*. 2024; 104(3): e202300733. Available from: https://doi.org/10.1002/zamm.202300733.

[34] Alqahtani AM, Khan MR, Akkurt N, Puneeth V, Alhowaity A, Hamam H. Thermal analysis of a radiative nanofluid over a stretching/shrinking cylinder with viscous dissipation. *Chemical Physics Letters*. 2022; 808: 140133. Available from: https://doi.org/10.1016/j.cplett.2022.140133.

[35] Khashi'ie NS, Arifin NM, Pop I, Wahid NS. Flow and heat transfer of hybrid nanofluid over a permeable shrinking cylinder with Joule heating: A comparative analysis. *Alexandria Engineering Journal*. 2020; 59(3): 1787-1798. Available from: https://doi.org/10.1016/j.aej.2020.04.048.

[36] Turkyilmazoglu M, Pop I. Exact analytical solutions for the flow and heat transfer near the stagnation point on a stretching/shrinking sheet in a Jeffrey fluid. *International Journal of Heat and Mass Transfer*. 2013; 57(1): 82-88. Available from: https://doi.org/10.1016/j.ijheatmasstransfer.2012.10.006.

[37] Khashi'ie NS, Arifin NM, Pop I, Wahid NS. Flow and heat transfer of hybrid nanofluid over a permeable shrinking cylinder with Joule heating: A comparative analysis. *Alexandria Engineering Journal*. 2020; 59(3): 1787-1798. Available from: https://doi.org/10.1016/j.aej.2020.04.048.